ACS APPLIED ENERGY MATERIALS

www.acsaem.org Article

In Situ Aniline-Polymerized Interfaces on GO−PVA Nanoplatforms as Bifunctional Supercapacitors and pH-Universal ORR Electrodes

Josiel J. Barrios Cossio, Próspero Acevedo Peña, Agileo Hernández-Gordillo, Luis F. Desdín García, Alain R. Puente Santiago,* Luis Echegoyen,* and Edilso Reguera*

Cite This: https://dx.doi.org/10.1021/acsaem.0c00361 Read Online

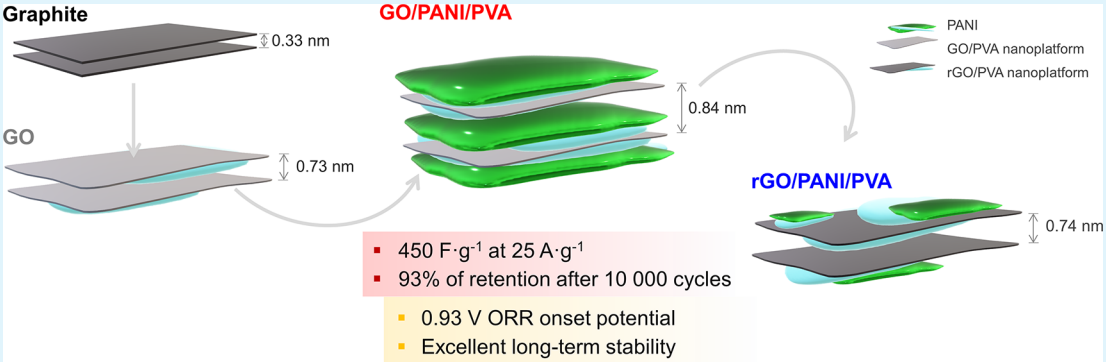

ABSTRACT: We report unique additive-free bifunctional electrodes, composed of graphene oxide (GO), reduced GO (rGO), polyaniline (PANI), and poly(vinyl alcohol) (PVA) on carbon cloths, which were fabricated using an easy and innovative in situ aniline polymerization strategy under mild conditions. The resulting electrodes were tested for energy storage and energy conversion reactions, and they exhibited competitive bifunctional supercapacitor and pH-universal oxygen reduction reaction (ORR) properties. Surprisingly, GO/PANI/PVA electrodes delivered a significant specific capacitance of 450 $F \cdot g^{-1}$ at a current density of 25 $A \cdot g^{-1}$, an ultrahigh cycling stability of 93% after 10 000 cycles of charge−discharge at 10 $A \cdot g^{-1}$, and an outstanding ORR onset potential value of 0.93 V vs reversible hydrogen electrode (RHE) in basic media. Additionally, the nanocomposite showed remarkable stability in acid media for the electroreduction of oxygen, maintaining 98% of the initial current applied after 25 000 s. The impressive performance of GO/PANI/PVA electrodes was attributed to their excellent electron-transfer (ET) properties, improved conductivity, and the highly stable behavior of PANI-functionalized GO layers.

KEYWORDS: *graphene oxide, polyaniline, poly(vinyl alcohol), supercapacitor, oxygen reduction reaction*

■ INTRODUCTION

The development of high-performance electrochemical technologies for energy storage and conversion is a top priority in modern society. The global environmental and energy crisis has triggered the design and fabrication of highly stable and efficient nanomaterials for supercapacitors (SCs) and water-splitting applications.[1] In this regard, the fabrication of ultrathin, wearable, and flexible SCs has greatly impacted the energy storage market due to their unbeatable properties, such as high power density, ultrahigh cycling stability, and very fast charge−discharge processes. The SC market is expected to reach U.S. $2.18 billion by 2022, mostly for consumption and automotive applications. To meet this huge demand, several strategies have been adopted to synthesize innovative materials with enhanced supercapacitive properties, including a myriad of different types of nanocarbons,[2,3] transition-metal dichalcogenide-based nanocomposites,[4] conductive polymers,[5] metal oxide−hydroxide nanoparticles,[6] and even metal−organic frameworks (MOFs).[7−9] In parallel, the development of high-performance water-splitting electrocatalysts to replace Pt-based materials as sustainable and clean energy conversion technologies has let to an impressive growth in recent years.[10] Special interest has been paid to develop oxygen reduction reaction (ORR) metal-free electrocatalysts, such as N-doped nanocarbons, as potential candidates for fuel cell cathode electrodes.[11,12]

The design of versatile bifunctional materials with increased supercapacitive behavior and remarkable ORR activities is an important goal in materials science. Among the most suitable

Received: February 18, 2020
Accepted: April 9, 2020
Published: April 9, 2020

nanostructured materials, graphene oxide (GO)-based nanocomposites offer a wide portfolio of tunable physical and chemical properties and have been recently used to fabricate highly efficient bifunctional nanomaterials for energy storage and conversion applications in aqueous media.[13,14] The incorporation of conductive polymers such as polyaniline (PANI) onto GO nanoplatforms to form three-dimensional (3D) interconnected network architectures has given rise to unique multifunctional electrodes, which facilitate faster ion diffusion and charge-transfer processes at the double layer, as well as an increase in the number of electrocatalytic active sites through the N atoms.[15] To create these nanostructured materials, several methodologies have been proposed, such as electrochemical polymerization,[16,17] electrophoretic deposition processes, and electrodeposition methods. However, the role of the nanoscale interactions at the interface between PANI and GO, together with the influence of the electrolyte on the performance of the resulting nanocomposites, has been barely investigated.[18] The very strong interactions between PANI and GO can directly influence the electrochemical properties of the GO/PANI nanohybrids. Also, the addition of poly(vinyl alcohol) (PVA) to the GO nanoplatforms could improve the electrolyte−nanocomposite interactions in aqueous media, facilitating the ion migration processes.

The development of bifunctional materials for energy storage and energy conversion applications has been scarcely reported up to now. In this work, additive-free GO and reduced GO (rGO)/PANI/PVA nanocomposites were prepared as bifunctional supercapacitors and pH-universal ORR electrodes using an innovative bottom-up in situ aniline polymerization strategy. Our approach uses 100% of the active material to manufacture the electrodes, avoiding the typical drawbacks commonly observed for those applications that add 30% of additives (carbon black and poly(vinylidene difluoride) (PVDF)),[2−7] which significantly decrease the electrochemical performance. The electrostatic interactions at GO/PANI interfaces controlled both the PANI distribution pattern and the electrical conductivity of the resulting nanohybrids, while PVA increased the ion accessibility. Consequently, the electrochemical performances of the nanocomposites for energy storage and energy conversion applications were mainly tuned by the GO/PANI and rGO/PANI interfacial interactions.

■ MATERIALS AND METHODS

Synthesis of Materials. The starting material was graphite (Sigma-Aldrich, 99.99%). A series of analytical-grade reagents (sulfuric acid, 95.0−98.0%; sodium nitrate, ≥99.0%; potassium permanganate, ≥99.0%; hydrogen peroxide solution, 30 wt % in H_2O; ethyl alcohol; aniline, ≥99.5%; sodium persulfate, ≥98%; hydrazine anhydrous, 98%; and poly(vinyl alcohol), M_w 85 000−124 000, 99+% hydrolyzed) were used as received from Sigma-Aldrich without further purification. Graphene oxide (GO) was synthesized from graphite as described below:[19] 1 g of graphite sample was oxidized using 51 mL of concentrated H_2SO_4, 1 g of $NaNO_3$, and 300 mL of H_2O_2. The resulting GO in suspension was filtered, washed several times with deionized water, and dried.

Afterward, the formation of the composite was initiated by the addition of GO into a poly(vinyl alcohol) (PVA) dispersion (2.5 g·L^{-1}) and sonicated for 1 h. Then, 35 μL of aniline in 1 mL of 1 M H_2SO_4 was added into 50 mL of GO/PVA dispersion and sonicated for 1 h more. Subsequently, 142.84 mg of $(NH_4)_2S_2O_8$ in 1 mL of 1 M H_2SO_4 was added into the dispersion with continuous stirring. After approximately 5 min, the mixture exhibited a green color, indicating polyaniline (PANI) formation. This mixture was separated into two equal parts: the first part (GO/PANI/PVA) was centrifuged, washed with deionized water, and dried at room temperature; the second part was reduced using hydrazine and then centrifuged, washed, and dried under the same conditions as described above (rGO/PANI/PVA).

Structural Characterization. Graphite, GO, GO/PANI/PVA, and rGO/PANI/PVA were characterized via Thermo Scientific DXR Raman spectroscopy to study their vibrational properties. During the measurements, a 10× objective (N/A 0.25) and solid-state laser at 532 nm (5 W) as excitation source were used (2 s of exposure time and 20 scans for each recorded spectrum). The X-ray diffraction (XRD) patterns of powders of graphite, GO, GO/PANI/PVA, and rGO/PANI/PVA were recorded on a D8 Advance (Bruker) X-ray diffractometer in the 50−70°/2θ angular range using Cu Kα radiation (40 kV, 20 mA).

The thermogravimetric curves were recorded under a dried nitrogen flow, using a high-resolution TGA Q5000 IR apparatus (from TA Instruments) operated at a heating rate of 10 °C·min^{-1}. The X-ray photoelectron spectroscopy (XPS) analyses were performed at room temperature using a K-Alpha+ spectrometer from Thermo Scientific Co. equipped with a monochromatic Al Kα X-ray source. The XPS regions were recorded at 20 eV pass energy with a step size of 0.1 eV. Curve fitting was performed with a Lorentzian−Gaussian (Voigt) peak shape and the Shirley method to remove the spectral background. The instrument work function was calibrated to give a binding energy (BE) of 83.96 eV for the Au $4f_{7/2}$ line for metallic gold, and the spectrometer dispersion was adjusted to give a BE of 932.62 eV for the Cu $2p_{3/2}$ line of metallic copper. Spectra were charge-corrected with the mainline of the carbon 1s spectrum (adventitious carbon) set to 284.8 eV. Spectra were analyzed using the Casa XPS software (version 2.3.14). The morphology of the composites was characterized using a JEOL HRTEM ARM 200 F operated at 200 keV. The elemental composition was determined by EDX Oxford Aztec. The samples were placed on copper grids.

Electrode Manufacturing. The working electrodes for energy storage characterization were manufactured using a carbon cloth 1 cm wide × 2 cm long (FuelCellStore). Subsequently, the pieces of carbon fabric were activated using 0.1 M H_2SO_4 in an ultrasonic bath for 30 min to impart some degree of hydrophilicity to the cloth. The mixtures of GO/PANI/PVA and rGO/PANI/PVA were dispersed (1 mg·mL^{-1}) and deposited on the carbon cloth dropwise, allowing it to dry at room temperature before adding the next drop. For this procedure, a graduated micropipette was used to add a total mixture volume of 9 μL to a piece of carbon cloth, ensuring that all of the mixture was deposited on an approximate area of 1 cm^2. The rest of the carbon cloth was masked using a Kapton tape to demarcate the deposition area. After adding nine drops (1 μL each), the area (1 cm^2) was completely covered. Two additional electrodes were manufactured: one by adding the dispersion of GO in PVA and forming GO/PVA nanoplatforms, and another using the GO/PVA dispersion after a reduction process with hydrazine (rGO/PVA nanoplatforms) (see Figure S1, Supporting Information). Three electrodes of each type were prepared to establish reproducibility.

Electrochemical Measurements. The materials supported on the carbon cloth were employed as working electrodes, and a Ag/AgCl (0.1 M, KCl) electrode and a graphite rod were used as reference and counter electrodes, respectively. A 1 M H_2SO_4 solution was employed as electrolyte after deoxygenation under an Ar flow. Cyclic voltammetry (CV) was used to determine the capacitance potential range of the electrodes and to estimate the diffusion-controlled and nondiffusion-controlled currents measured for the materials. CV and linear sweep voltammetry were used for electrocatalysis measurements using an oxygen gas (O_2) flow. Electrochemical impedance spectroscopy (EIS) was employed to measure the film resistances and capacitances in the potential range established by CV, as previously described.[20] In brief, the working electrode is polarized at its uppermost potential, and this is maintained until a stable current is reached. Then, an EIS spectrum is recorded in the frequency range from 100 kHz to 10 mHz with a

https://dx.doi.org/10.1021/acsaem.0c00361
ACS Appl. Energy Mater. XXXX, XXX, XXX−XXX

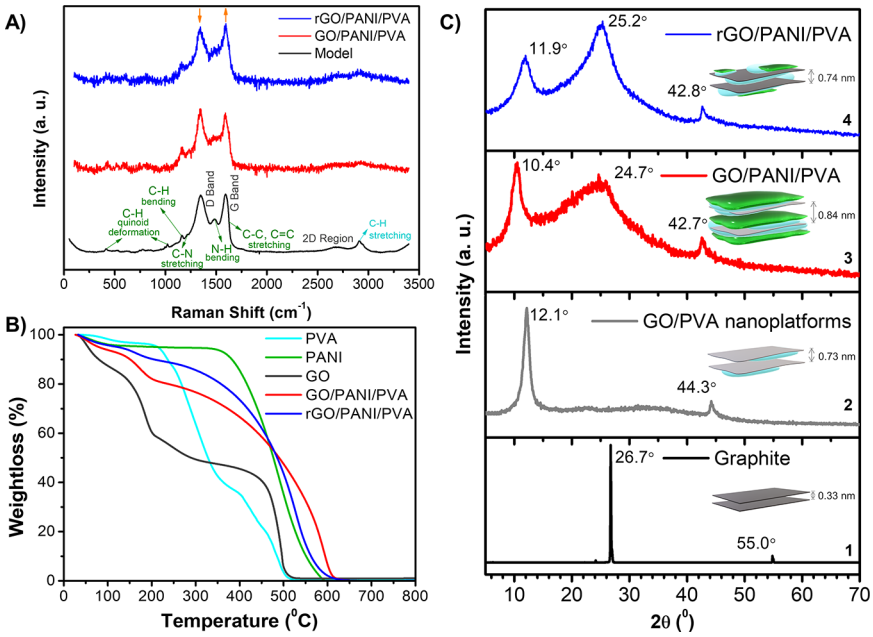

Figure 1. Raman spectra of an experimentally constructed model (black) compared with GO/PANI/PVA (red) and rGO/PANI/PVA (blue) (A); thermogravimetric curves of PVA (light blue), PANI (green), GO (gray), GO/PANI/PVA (red), and rGO/PANI/PVA (blue) (B); and X-ray diffraction patterns of graphite (black), GO (gray), GO/PANI/PVA (red), and rGO/PANI/PVA (blue). (C) XRD pattern of GO, rGO, and the resulting nanocomposites.

sinusoidal ac perturbation of ±10 mV. After this, the electrode potential is shifted (ν = 0.16 mV·s^{-1}) toward the next measuring potential. The measurement is continued until the whole potential range is scanned in a forward and backward direction. Galvanostatic charge−discharge (GCD) curves were employed to determine the specific capacitance of the electrodes and to characterize the film stability under long-term cycling. A Metrohm Autolab Multichannel Potentiostat/Galvanostat Instrument (M204) was employed for this purpose.

■ RESULTS AND DISCUSSION

Structural Characterization. Raman spectroscopy, XRD, thermogravimetric analysis (TGA), transmission electron microscopy (TEM), and XPS were used to evaluate the qualitative structural features of the as-synthesized nanocomposites. Figure 1A shows the Raman spectra of the GO/PANI/PVA (red) and rGO/PANI/PVA (blue) materials compared with an experimental model (black). The experimental model was constructed by adding the experimental Raman spectra of the GO, PANI, and PVA substances, whose intensities were normalized and multiplied by their respective fractions in the mixtures (0.7, 0.2, and 0.1) (see Figure S2, Supporting Information). As expected, both materials showed similar Raman features. In this regard, taking into account the aniline polymerization mechanism, the covalent functionalization of PANI onto the GO/PVA nanoplatform did not occur or occurred with a very low yield.[21,22] The polymer formed should be distributed around the GO−PVA nanoplatforms. For this reason, it is expected that the composites (GO/PANI/PVA and rGO/PANI/PVA) will exhibit Raman signals corresponding to GO, rGO, PANI, and PVA vibrational properties, which are affected by the electrostatic interactions among the individual components.

The Raman spectrum of GO (Figure 1A) shows intense D (1369 cm^{-1}) and G bands (1576 cm^{-1}); furthermore, at the high wavenumber region, the 2D waves can be observed (2400−3250 cm^{-1}).[23] The D band presence is due to defects in the carbon's crystalline curved structure, and its higher intensity is as a result of a high structural disorder, which is caused essentially by the presence of oxygen functional groups on the GO and rGO surfaces.[23] The G band corresponds to the in-plane optical mode of vibration for two adjacent sp^2 carbon atoms on an ideal hexagonal ring of graphite.[24] The combined tones for the peaks located at 2670 cm^{-1} (2D) and 2925 cm^{-1} (D + G) constitute the 2D region. This 2D region reflects two-photon processes involving phonons with opposite wave vectors.[24] However, the strengthening of the intensity of the D + G band region is probably due to the contribution of a band with a maximum at 2917 cm^{-1}. This band is attributed to valence C−H vibrations in the PVA spectrum.[25] It is interesting to note that the I_D/I_G ratio in the rGO/PANI/PVA spectrum is lower than the I_D/I_G ratio in the GO/PANI/PVA spectrum, indicating the loss of oxygenated functional groups during the reduction step.[21,26]

Raman results also show a large group of signals derived from the PANI. In the low wavenumber region (Figure 1A) with mid-intensity, a 525 cm^{-1} band (amine in-plane deformation) and two bands at 748 and 775 cm^{-1}, respectively, are associated with imine deformation (C−H bending).[27] There are very strong intense bands at 1161 cm^{-1} (C−H bending in emeraldine form), 1213 cm^{-1} (C−N stretching in emeraldine form (amines)), 1488 cm^{-1} (C═N stretching in emeraldine base (imines)), which are observed between the G and D bands of the GO, and at 1584 cm^{-1} (C−C stretching in benzene-type ring and C═C stretching in quinone-type ring) overlapped with the D band of GO.[27,28] Additionally, practically all of the main Raman bands of GO/PANI/PVA and rGO/PANI/PVA materials are shifted to lower values compared with the bands in the model spectrum, which is a consequence of strong noncovalent interactions between the individual components of the nanohybrids.[29,30]

Figure 1B shows the thermogravimetric curves of PVA, PANI, GO, and the mixtures GO/PANI/PVA and rGOPANI/

https://dx.doi.org/10.1021/acsaem.0c00361
ACS Appl. Energy Mater. XXXX, XXX, XXX−XXX

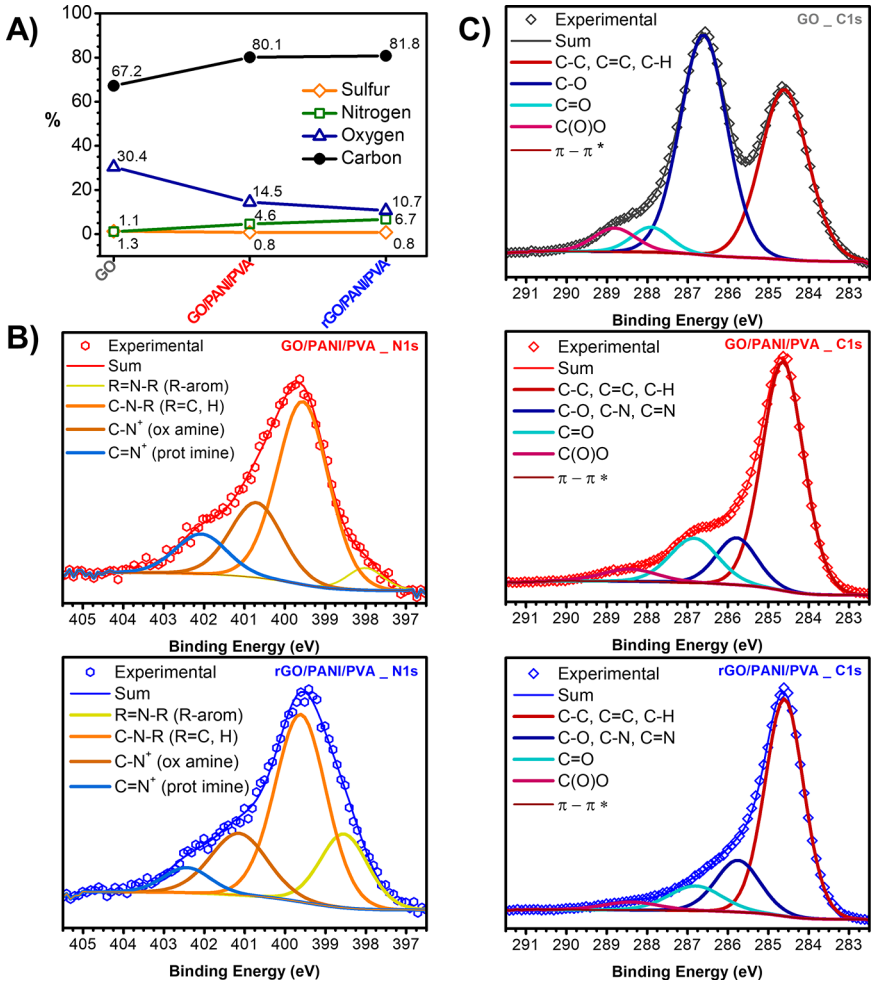

Figure 2. Atomic content in percent of carbon, oxygen, nitrogen, and sulfur of the GO, GO/PANI/PVA, and rGO/PANI/PVA materials derived from XPS data (A). High-resolution N 1s XPS spectra of GO/PANI/PVA and rGO/PANI/PVA (B) and high-resolution C 1s XPS spectra of GO, GO/PANI/PVA, and rGO/PANI/PVA (C).

PVA. Most of the structures (PANI, PVA, GO/PANI/PVA, and rGO/PANI/PVA) exhibit a low mass loss (<10%) and GO (20%) of around 100 °C, due to water deintercalation and evaporation.[31,32] PVA shows its typical five-step degradation curve after water loss: one phase transition at 206−224 °C. The largest mass loss (∼60%) occurs between 120 and 340 °C due to the dehydration of vicinal hydroxyl groups with elimination of water and defunctionalization reactions, and two final overlapped processes that correspond to chain decomposition reactions at around 335 °C.[32] GO continues to lose mass until 300 °C due to the decomposition of the oxygen functional groups and at around 300 °C PANI decomposition begins. Compared with the GO curve, GO/PANI/PVA and rGO/PANI/PVA begin their decomposition at a similar temperature but show better thermal stability, which could be attributed to the decomposition of the PANI component. However, GO/PANI/PVA is slightly more stable than rGO/PANI/PVA, probably due to a stronger electrostatic interaction between the functional groups of the GO and PANI components.

Figure 1C shows the diffraction patterns obtained in the range of 2θ from 5 to 70° for the powder samples of graphite, GO, GO/PANI/PVA, and rGO/PANI/PVA. All of these patterns exhibit a first diffraction peak that indicates the distance between graphene (graphite) and graphene oxide (GO, GO/PANI/PVA, and rGO/PANI/PVA) layers. The shortest distance is exhibited by graphite 2θ = 26.7°, which is correlated to an interlayer spacing of 0.33 nm, denoting a typical strong graphite π−π interaction. GO shows a larger interlayer spacing than graphite (0.73 nm and 2θ = 12.1°), which confirms the exfoliation of GO due to the attachment of oxygenated groups and the presence of layers of water in the inner space of the material.[33] Likewise, GO/PANI/PVA exhibits a larger interlayer spacing than GO (0.84 nm and 2θ = 10.4°); this increment in the interlayer spacing is observed due to the intercalation of PANI between GO sheets. On the other hand, rGO/PANI/PVA displays its first diffraction peak at 11.9°, which corresponds to an interlayer distance of 0.74 nm, slightly longer than that for GO, presumably caused by the deintercalation of PANI from GO sheets induced by the reduction process of GO. The second peak in GO/PANI/PVA (24.7°) and rGO/PANI/PVA (25.2°) patterns indicates the formation of PANI, and the third peak in GO/PANI/PVA (42.7°) and rGO/PANI/PVA (42.8°) patterns, as well as the second peak in GO (44.1°) and graphite (55.4°) patterns, indicates a short-range order in stacked graphene oxide and graphene layers.[34]

According to Zou et al.,[18] it is important to assess the interactions and reactions between GO and PANI in graphene/PANI composites because they have a significant

https://dx.doi.org/10.1021/acsaem.0c00361
ACS Appl. Energy Mater. XXXX, XXX, XXX−XXX

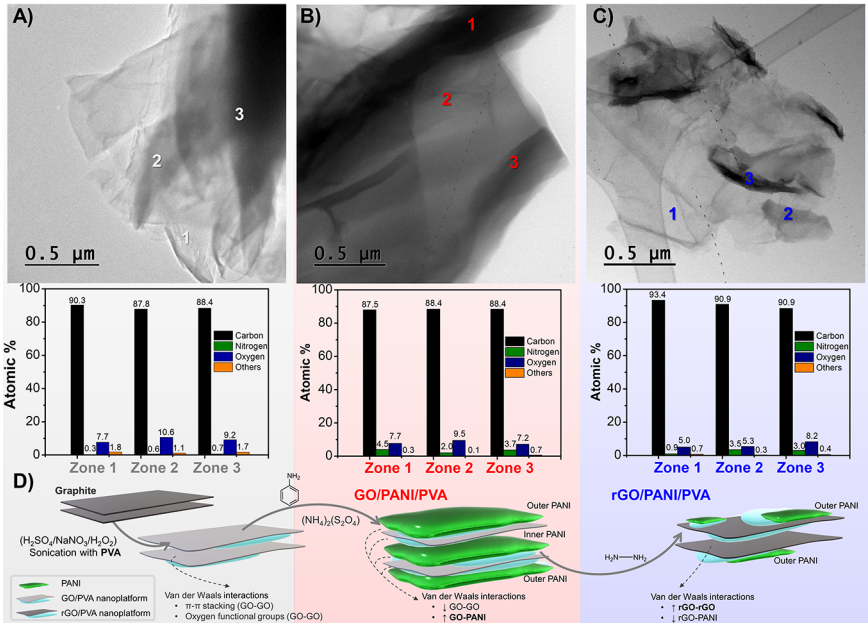

Figure 3. Transmission electron microscopy (TEM) images and elemental composition analysis derived from EDS analysis, taken in GO (A), GO/PANI/PVA (B), and rGO/PANI/PVA (C) materials. Schematic representation of the synthesis process followed and the possible final structure of composites (D), according to the data obtained from the structural characterization.

influence on the final electrochemical performance. In this sense, the interpretation of the X-ray photoelectron spectra (XPS) of GO, GO/PANI/PVA, and rGO/PANI/PVA can provide a lot of valuable structural insights (Figure 2). Figure 2A shows the total content of the main element (C, O, N, and S) components in GO, GO/PANI/PVA, and rGO/PANI/PVA, estimated by XPS (see Figure S3, Supporting Information). The approximately constant content of sulfur and the appearance of S 2p peaks in each composite (see Figure S3, Supporting Information) may derive from H_2SO_4, used during all synthesis procedures. Figure 2A shows the increased content of N together with the decreased content of O, which can be attributed to both the addition of PANI to GO/PANI/PVA and rGO/PANI/PVA and the reductive process of GO/PANI/PVA to rGO/PANI/PVA, respectively.

Figure 2B shows the nitrogen 1s XPS of GO/PANI/PVA and rGO/PANI/PVA composites that can be deconvoluted into four signals. The first and the second signals correspond to quinonoid imine (R═N−R, R-arom) and benzenoid amine (C−N−R, R = C, H) environments, centered at ∼398 and ∼399.5 eV, respectively. The third (∼400.9 eV) and fourth (∼402.2 eV) signals can be attributed to positively charged nitrogens: oxidized amine ($C-N^+$) and protonated imine ($C{=}N^+$), respectively.[18,35,36] All of these signals correspond to PANI and allow the determination of the polymer oxidation state and doping level, which are very important factors affecting PANI properties, mainly, its electrical conductivity.[37] The oxidation state can be determined by the quinonoid imine/benzenoid amine ratio (Q/B) and the doping level by the positively charged nitrogen/total nitrogen ratio (N^+/N_T).[18] It is possible to demonstrate from the N 1s XPS that GO/PANI/PVA (Q/B = 0.09, N^+/N_T = 36.8) has a more oxidized PANI and doped level than rGO/PANI/PVA (Q/B = 0.37, N^+/N_T = 26.2), which means that the PANI in rGO/PANI/PVA must have a lower conductivity.[18] The doping level influences the strength of the electrostatic interaction between GO, rGO, and PANI, being stronger for GO/PANI/PVA, due to the higher surface charge density in the PANI polymeric network.

The deconvolution of C 1s peaks of GO (Figure 2C) results in four main components: nonoxygenated (C−C, C═C, C−H) at ∼284.6 eV, C−O bonds (∼286.6 eV), carbonyl (∼287.9 eV), and the carboxylate component (O−C═O) at ∼289.0 eV. Although the high-resolution C 1s spectra of GO/PANI/PVA and rGO/PANI/PVA also exhibit three similar signals corresponding to the nonoxygenated (C−C, C═C, C−H), carbonyl (C═O), and carboxylate (O−C═O) components, the other component (C−O bonds) is slightly modified due to the overlapping of C−N and C═N contributions (Figure 2C).[38] The high-resolution spectra of O 1s (see Figure S3C, Supporting Information) for GO, GO/PANI/PVA, and rGO/PANI/PVA always show the same three signals, corresponding to C−OH (∼533.4 eV), C═O (∼532.3 eV), and COOH (∼531.2 eV).[39]

The morphological and compositional characterization of the composites was performed by TEM (see Figure 3). GO is observed as wrapped graphene oxide sheets with some dark regions originated by the stacking of several layers (see Figure 3A). Energy-dispersive spectrometry (EDS) analysis at three different points of the sample confirms the presence of a huge number of oxygenated groups, which is characteristic of this material. Meanwhile, GO/PVA/PANI seems to be composed of several stacked layers since a dark image of the material is obtained (see Figure 3B). EDS analysis shows an overall increment in nitrogen content in this composite in comparison with that of GO. These nitrogen species come from PANI incorporated in the material, evidencing that this polymer is homogeneously distributed over the GO sheets. Then, GO/PVA/PANI is composed of layers of GO−PVA nanoplatforms covered with PANI, stabilized on GO surfaces via $\pi-\pi$ stacking.[40] It is worth pointing out that GO/PVA/PANI also contains a large number of oxygenated groups, proving that functional groups from GO are maintained after composite formation. Actually, oxygen-containing functional groups are

https://dx.doi.org/10.1021/acsaem.0c00361
ACS Appl. Energy Mater. XXXX, XXX, XXX−XXX

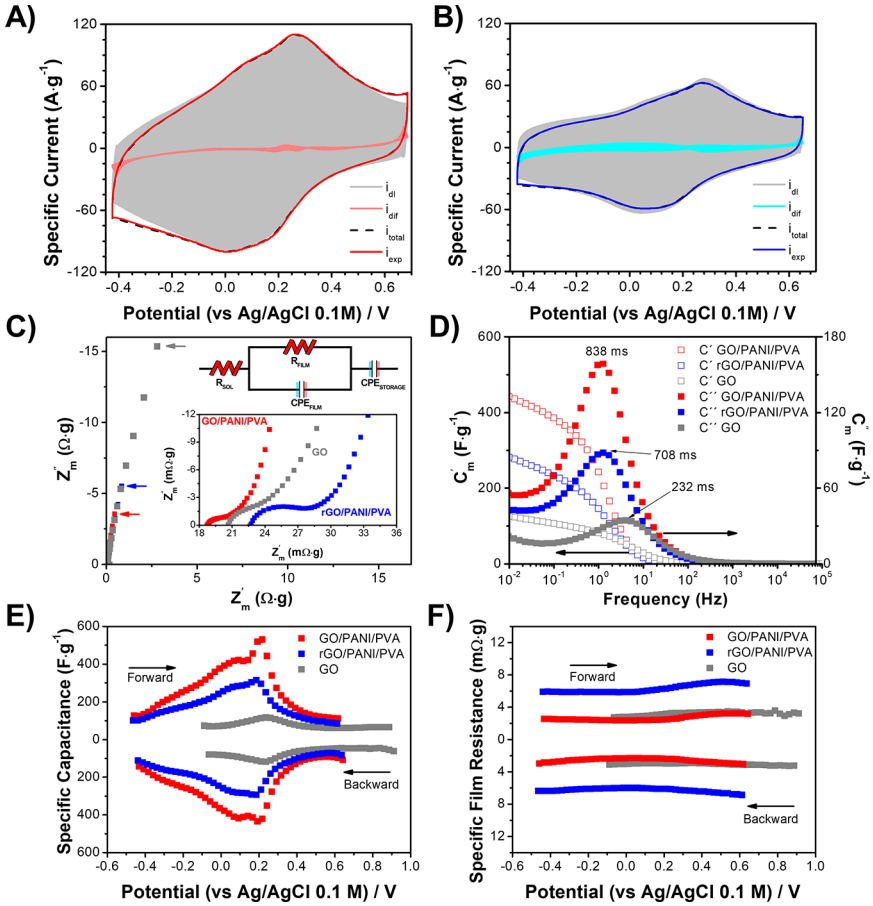

Figure 4. Cyclic voltammetry characterization (ν = 250 mV·s^{-1}) of (A) GO/PANI/PVA and (B) rGO/PANI/PVA electrodes. Typical (C) Nyquist and (D) real (C'') and imaginary (C') capacitance plots measured (E = 0.2 V) for GO/PANI/PVA, rGO/PANI/PVA, and GO electrodes. Impact of measuring potential on the (E) specific capacitance and (F) film resistance for GO/PANI/PVA, rGO/PANI/PVA, and GO electrodes, derived from the best fit of the equivalent circuit (inset in (C)). All of these results were obtained in a deoxygenated 1 M H_2SO_4 solution.

active sites for polymerization.[41] Surprisingly, rGO/PVA/PANI is composed of GO layers, with some agglomerates observed as darker regions. EDS analysis indicates that darker regions are originated by the presence of PANI since the N content is increased. The oxygen content in this composite is also lower than in GO and GO/PVA/PANI, which is due to the partial reduction of GO in this composite. However, the oxygen content is considerably higher in the dark regions, indicating the presence of PVA or the preservation of remnant oxygen functional groups.

Energy Storage Properties. The energy storage properties of the composites were studied in a 1 M H_2SO_4 solution using electrochemical techniques. The capacitive potential range was selected from cyclic voltammetry. Each composite exhibits a slightly different window depending on its composition. GO/PANI/PVA and rGO/PANI/PVA show reversible redox reactions in a potential window characteristic for PANI-based materials;[42−45] see Figure 4A,B. Both composites show a box-like electrochemical fingerprint with the contribution of the emeraldine/pernigraniline redox process, detected as current peaks close to 0.2 V. However, the measured currents for GO/PANI/PVA are considerably higher than those for rGO/PANI/PVA.[46] Figure S1 shows a comparison of CV of GO/PVA and rGO/PVA composites with GO/PANI/PVA and rGO/PANI/PVA. The presence of PANI in the nanoplatforms is the source of the high capacitances measured. Moreover, the dramatic increment of capacitance when PANI is coupled with GO/PVA, in comparison with that obtained for rGO/PVA, evidence for a synergistic interaction between these materials promoted by a strong PANI−GO interaction through oxygenated functional groups. Figure 4A,B also shows the contribution of diffusion-controlled (i_{DC}) and non-diffusion-controlled (i_{NDC}) processes to the measured current (i_{exp}), estimated by using equation $i_{total} = i_{DC} + i_{NDC} = A\nu^{0.5} + B\nu$,[47,48] where ν represents the scan rate, and A and B are the proportionality coefficients for diffusion-controlled and non-diffusion-controlled processes, respectively. The measured currents for both composites are mainly from nondiffusion-controlled processes, superficial or fast redox processes, and double-layer charging−discharging. This result makes GO/PANI/PVA and rGO/PANI/PVA suitable materials for supercapacitors. Similar results have been reported for PANI−GO-based composites.[49,50]

Typical Nyquist diagrams obtained for GO, GO/PANI/PVA, and rGO/PANI/PVA are shown in Figure 4C. A semicircle is observed in the high-frequency regime (inset figure), commonly associated with the resistance and capacitance of film components. An almost linear increment of the imaginary impedance is registered in the middle- and low-frequency regimes, associated with charge storing processes in the film (capacitance). The magnitude of the impedances depends on film composition and measuring potentials, but, in general, lower impedances are measured for GO/PANI/PVA film. Real (C') and imaginary (C'')

https://dx.doi.org/10.1021/acsaem.0c00361
ACS Appl. Energy Mater. XXXX, XXX, XXX−XXX

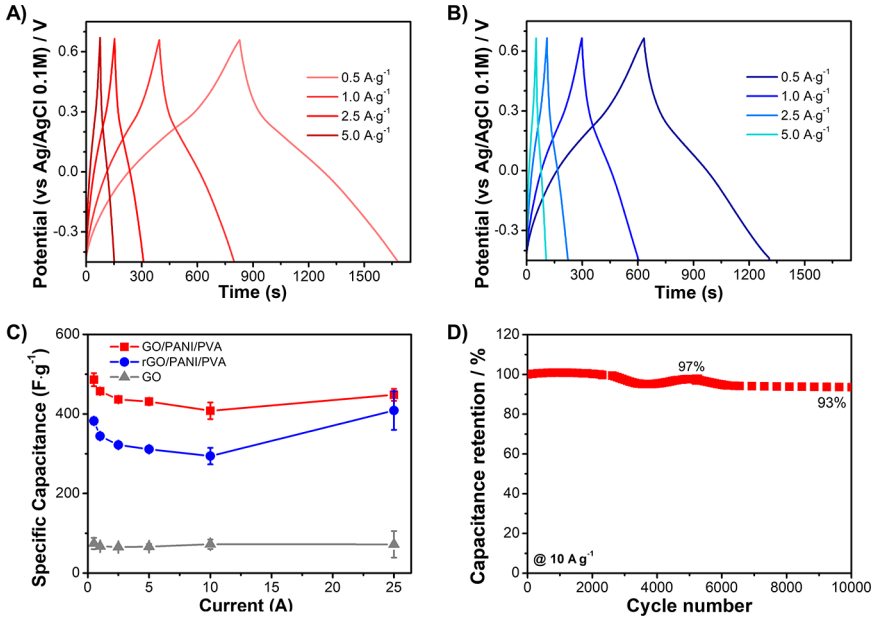

Figure 5. Galvanostatic charge–discharge curves measured in a deoxygenated 1 M H_2SO_4 solution at different currents, for GO/PANI/PVA (A) and rGO/PANI/PVA (B) electrodes. Impact of the imposed current over the specific capacitance of GO/PANI/PVA, rGO/PANI/PVA, and GO electrodes (C). Capacitance retention recorded for GO/PANI/PVA electrode at a current of 10 $A{\cdot}g^{-1}$ (D).

capacitances for the films, as a function of measuring frequency, are shown in Figure 4D. The composites exhibit considerably larger C' values at low frequencies than GO, because of the contribution of PANI and the structural modification of the composites. However, when GO is present in the composite, higher capacitance values (up to 1.5 times larger) are obtained. This improvement is associated with the arrangement of GO sheets and PANI layers achieved by the π–π stacking, the more effective interaction promoted by the presence of oxygenated functional groups, and the improved electronic conductivity expected for PANI in this composite. Time constant values can be obtained at the frequency at which the maximum C'' is registered. This value is larger for composites than for GO, due to the increment in capacitance.[51] Nevertheless, between both composites, there is only a slight difference in this parameter. This behavior might be related to the better electronic transport through this composite, allowing a similar time response with improved capacitance. The time constant values are almost the same through the whole potential window for GO/PANI/PVA and rGO/PANI/PVA (see Figure S4, Supporting Information), confirming that the redox processes of PANI exhibit fast kinetics.

Film capacitance (Figure 4E) and resistance (Figure 4F) for electrodes made of GO, GO/PANI/PVA, and rGO/PANI/PVA were derived by fitting experimental EIS spectra to the equivalent electric circuit inserted in Figure 4C. Variation of film capacitance with potential resembles the CV curves for the materials (see Figure 4A,B), confirming that large energies are stored when oxygenated functional groups of graphene in the composite are preserved in the composite. The main differences in the composites' capacitances are around the potential at which the PANI redox process is expected. Therefore, the larger currents measured for GO/PANI/PVA might be caused by a more homogeneous distribution of PANI on GO sheets, favored by the presence of oxygenated groups and the efficient interaction between PANI and GO/PVA nanoplatforms. Moreover, the film resistance for GO/PANI/PVA is up to 2.6 times lower than the film resistance for rGO/PANI/PVA, thus promoting charge transport and redox processes related to charge storage. This result is in line with the Q/B and N^+/N_T ratios derived from the XPS results. The improved behavior of GO/PANI/PVA is related to the stronger GO–PANI interaction favored by oxygen-containing functional groups and the π–π stacking between PANI and GO/PVA nanoplatforms.

Galvanostatic charge–discharge curves for GO/PANI/PVA and rGO/PANI/PVA, measured at different currents, are shown in Figure 5A,B, respectively. In both cases, an almost triangular shape is obtained, with a deviation from linearity due to the fast redox processes taking place in the PANI. Capacitances derived from the charge passed during the discharge are plotted in Figure 5C against the current employed for the measurement. The capacitance for both composites is considerably larger than that for the bare GO, as previously observed by EIS (Figure 4E). GO/PANI/PVA (486, 455, 435, 430, 405, and 450 $F{\cdot}g^{-1}$ at 0.5, 1, 2.5, 5, 10, and 25 $A{\cdot}g^{-1}$, respectively) exhibits larger capacitance values than rGO/PANI/PVA (382, 344, 322, 310, 297, and 408 $F{\cdot}g^{-1}$ at 0.5, 1, 2.5, 5, 10, and 25 $A{\cdot}g^{-1}$, respectively) in the whole current range employed for the measurements, as expected from the previous characterization. However, the capacitance for rGO/PANI/PVA increased considerably at high current, reaching values very close to those registered for GO/PANI/PVA. This behavior might be related to the fact that at these large currents the charge stored is mainly due to electrical double-layer charging, and the contribution from PANI is negligible. Composite capacitances are on the same order of magnitude, or even larger than the currently reported capacitances for PANI–GO-based composites.[41,46,49,50,52] Finally, the GO/PANI/PVA electrode was long-term-cycled at a current of 10 $A{\cdot}g^{-1}$ to evaluate the stability of this material (Figure 5D). The capacitance remained almost constant during the first 2500 cycles, showing a slight capacitance

https://dx.doi.org/10.1021/acsaem.0c00361
ACS Appl. Energy Mater. XXXX, XXX, XXX–XXX

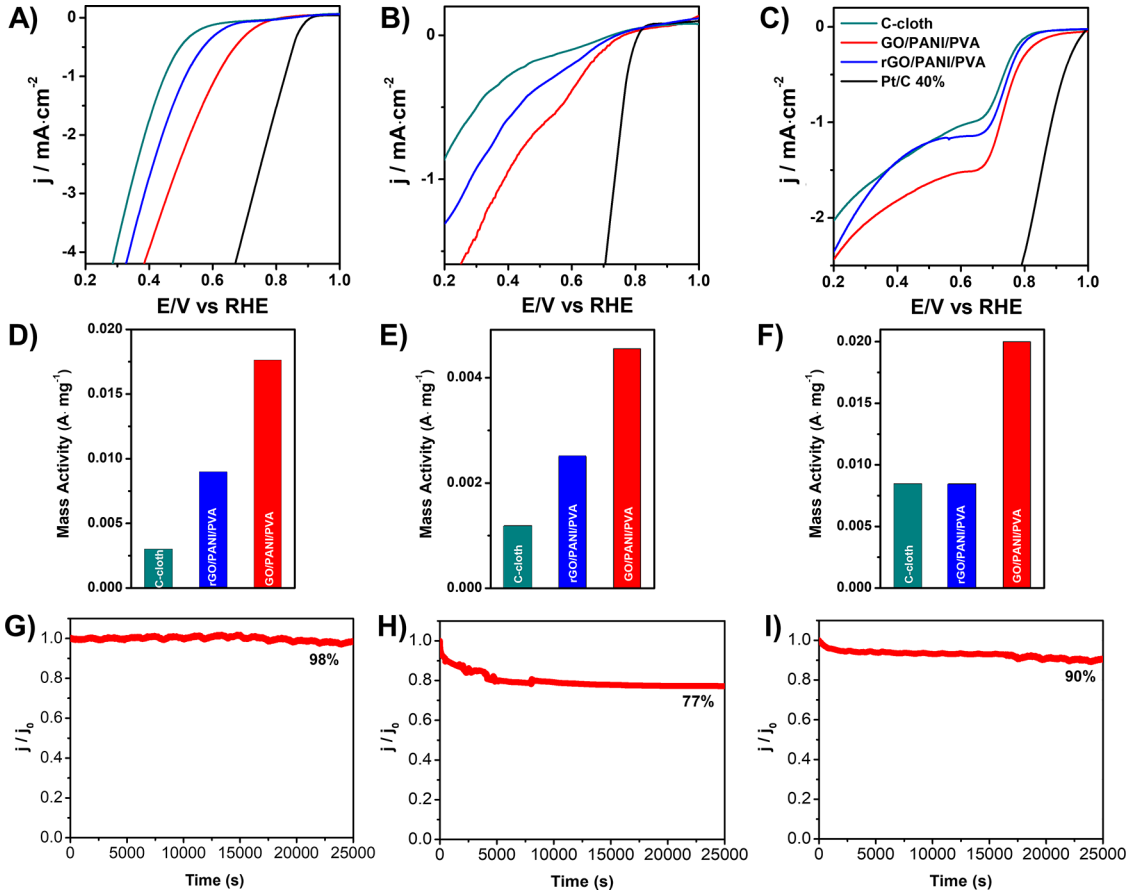

Figure 6. ORR polarization curves of the C-cloth, rGO/PANI/PVA, GO/PANI/PVA, and Pt/C (40%) in O_2-saturated solutions of (A) 0.5 M H_2SO_4, (B) phosphate buffer solution (pH = 7), and (C) 0.5 M NaOH. respectively. Scan rate: 5 mV·s^{-1}. The corresponding mass activity values of C-cloth, rGO/PANI/PVA, and GO/PANI/PVA in (D) acid, (E) neutral, and (F) basic pH values, respectively. Chronoamperometric curves at −0.35 V vs RHE of GO/PANI/PVA nanocomposites at (G) 0.5 M H_2SO_4, (H) PBS pH = 7, and (I) 0.5 NaOH.

decrease up to the 10 000th cycle, at which 93% of the original capacitance was retained.

Electrocatalytic Properties. The ORR activity of the GO-based nanocomposites was explored by cyclic voltammetry at different pH values for comparison. As shown in Figure S5 (Supporting Information), there are no electrochemical responses for the samples at different pH values in O_2-free NaOH solutions, while very well-defined oxygen reduction peaks appear under O_2-saturated conditions, indicating that the two nanocomposites efficiently enable the pH-universal oxygen reduction processes at the GO/PANI electrochemical interfaces. The synergistic interactions between the N-rich PANI polymeric networks and the highly conductive GO nanoplatforms provide both remarkable electron-transporting properties and a high number of active sites for oxygen adsorption to the resulting nanocomposites. Noticeably, positive shifts in the potential values of the oxygen reduction peaks were observed for GO/PANI/PVA compared with those for rGO/PANI/PVA at each pH, indicating an improvement of the electrocatalytic activity in the GO/PANI interfaces.

The ORR polarization curves of GO/PANI/PVA and rGO/PANI/PVA were evaluated at different pH values and compared with the results for commercial Pt/C (40 wt %) (Figure 6A−C). Remarkably, GO/PANI/PVA hybrids outperformed the electrocatalytic properties of rGO/PANI/PVA. Using unreduced GO materials, the onset potential was increased from 0.67 to 0.77 V, 0.75 to 0.77 V, and 0.84 to 0.93 V (vs reversible hydrogen electrode (RHE)) in acid, neutral, and basic environments, respectively. The N atoms from PANI may be acting like nitrogen-containing active sites in the carbon nanostructured networks.[53,54] It is worth to mention that, in basic solutions, the onset potential of the GO/PANI/PVA nanocatalyst is very close to that of the Pt/C reference and comparable to those of the state-of-the-art GO/PANI catalysts reported in the literature.[15,53,55] Additionally, the mass activity (Figure 6D−F), which represents a reliable measure of the electrocatalytic yield, is significantly boosted in the GO/PANI/PVA surfaces for each pH value, in agreement with the CV trends. However, unlike the reduced GO surfaces, the specific interactions between a large number of functional groups (carboxyl, ethoxy, etc.) of the GO nanosheets and aniline monomers gave rise to highly uniform and stable PANI layers (see Figure 3). The highly homogeneously distributed PANI layers could greatly enhance both the electron transfer (ET) through the nanocomposites and the number of ORR active sites of the GO/PANI/PVA 3D-layered structures. In this regard, XPS and EIS results demonstrated that both the electron conductivity and the ionic mass transfer are significantly improved for the GO/PANI interfaces, which become suitable electrochemical platforms for the efficient electrochemical reduction of oxygen. Bearing in mind these ideas, it is conceivable that the electrocatalytic behavior of the (r)GO/PANI interfaces is significantly affected by the GO−PANI interfacial interactions. Undoubtedly, a large number of

https://dx.doi.org/10.1021/acsaem.0c00361
ACS Appl. Energy Mater. XXXX, XXX, XXX−XXX

available functional groups at the GO surfaces, which can interact via van der Waals forces with the N atoms of the aniline moieties, facilitate the assembly of a well-distributed PANI layer with desirable electronic properties for ORRs.

The chronoamperometric measurements of GO/PANI/PVA were carried out to get insights into its long-term stability properties (Figure 6G−I). The nanocomposite showed remarkable stability in acid media, maintaining 98% of the initial current applied after 25 000 s, surpassing all of the carbon-based metal-free ORR electrocatalysts.[9] It could be mainly attributed to the outstanding stability of the PANI films toward the electrochemical reduction of oxygen films at −0.35 V vs RHE.

Remarkably, although PANI was used to fabricate high-performance N-doped carbon catalysts using heat treatment methods, the electrocatalysts constructed from conductive polymers without heat treatment have usually delivered very low ORR activities.[54,56] To the best of our knowledge, the GO/PANI/PVA constitutes the first example of a nonmetallic ORR electrocatalyst with outstanding catalytic properties based on PANI networks built under mild conditions. The excellent electron-transfer (ET) properties, improved conductivity, and highly stable behavior of PANI-functionalized GO layers enable the effective electronic wiring between the electrode and the adsorbed oxygen species and favor the accessibility of oxygen molecules onto the electrocatalytically active sites, which can in turn improve their catalytic and long-term stability properties.

■ CONCLUSIONS

Two nanostructured PANI-based composites were successfully prepared using a simple and innovative in situ aniline polymerization method and a subsequent reductive step. Noticeably, GO/PANI/PVA nanocomposites showed improved conductivity properties, as well as rather uniformly distributed PANI networks, which have been directly associated with the unique synergistic interactions at the PANI/GO interfaces between the N-rich polymeric structure and the functional groups at the GO surfaces. Therefore, the electrochemical performance of the GO/PANI/PVA nanohybrids surpassed by far the activity of the rGO/PANI/PVA. The composites showed improved specific capacitances of 450 $F \cdot g^{-1}$ at a current density of 25 $A \cdot g^{-1}$ and an ultrahigh cycling stability of ca. 93% after 10 000 cycles of charge−discharge at 10 $A \cdot g^{-1}$. Likewise, an outstanding ORR onset potential value of 0.93 V vs RHE in basic media and excellent long-term stability properties in acid and basic environments were obtained for the GO/PANI electrochemical interfaces. The synthesized GO/PANI/PVA electrodes supported on carbon cloths are promising candidates for the development of flexible and wearable supercapacitor devices, as well as efficient metal-free pH-universal ORR fuel cell cathode materials.

■ ASSOCIATED CONTENT

Supporting Information

The Supporting Information is available free of charge at https://pubs.acs.org/doi/10.1021/acsaem.0c00361.

Details on the process and synthesis of the electrodes, experimental construction of the Raman model, elemental XPS composition, and imaginary capacitance (C'') and CVs under Ar- and O_2-saturated solutions of the rGO/PANI/PVA and GO/PANI/PVA composites (PDF)

■ AUTHOR INFORMATION

Corresponding Authors

Alain R. Puente Santiago − *Department of Chemistry and Biochemistry, University of Texas at El Paso, El Paso, Texas 79968, United States;* orcid.org/0000-0002-8491-3565; Email: arpuentesan@utep.edu

Luis Echegoyen − *Department of Chemistry and Biochemistry, University of Texas at El Paso, El Paso, Texas 79968, United States;* orcid.org/0000-0003-1107-9423; Email: echegoyen@utep.edu

Edilso Reguera − *Instituto Politécnico Nacional, CICATA-Legaria, CP 11500 Mexico City, Mexico;* orcid.org/0000-0002-4452-9091; Email: edilso.reguera@gmail.com

Authors

Josiel J. Barrios Cossio − *Instituto Politécnico Nacional, CICATA-Legaria, CP 11500 Mexico City, Mexico*

Próspero Acevedo Peña − *CONACYT—Instituto Politécnico Nacional, CICATA-Legaria, CP 11500 Mexico City, Mexico*

Agileo Hernández-Gordillo − *Instituto de Investigaciones en Materiales, Universidad Nacional Autónoma de México, CP 04510 Mexico City, Mexico*

Luis F. Desdín García − *Centro de Aplicaciones Tecnológicas y Desarrollo Nuclear, Havana 11300, Cuba*

Complete contact information is available at: https://pubs.acs.org/10.1021/acsaem.0c00361

Notes

The authors declare no competing financial interest.

■ ACKNOWLEDGMENTS

J.J.B.C. would like to thank CONACYT for the master scholarship and the mobility grant (CONACYT project A1-S-9877). The authors thank Laboratorio Nacional de Conversion de Energia (LNCAE) for providing some infrastructure required to perform the project. The Robert A. Welch Foundation is also gratefully acknowledged for an endowed chair to Prof. Luis Echegoyen (grant AH-0033).

■ REFERENCES

(1) Kong, D.; Gao, Y.; Xiao, Z.; Xu, X.; Li, X.; Zhi, L. Rational Design of Carbon-Rich Materials for Energy Storage and Conversion. *Adv. Mater.* **2019**, No. 1804973.

(2) Borenstein, A.; Hanna, O.; Attias, R.; Luski, S.; Brousse, T.; Aurbach, D. Carbon-based composite materials for supercapacitor electrodes: a review. *J. Mater. Chem. A* **2017**, *5*, 12653−12672.

(3) Yang, Z.; Tian, J.; Yin, Z.; Cui, C.; Qian, W.; Wei, F. Carbon nanotube-and graphene-based nanomaterials and applications in high-voltage supercapacitor: A review. *Carbon* **2019**, *141*, 467−480.

(4) Cherusseri, J.; Choudhary, N.; Kumar, K. S.; Jung, Y.; Thomas, J. Recent trends in transition metal dichalcogenide based supercapacitor electrodes. *Nanoscale Horiz.* **2019**, *4*, 840−858.

(5) Meng, Q.; Cai, K.; Chen, Y.; Chen, L. Research progress on conducting polymer based supercapacitor electrode materials. *Nano Energy* **2017**, *36*, 268−285.

(6) Owusu, K. A.; Qu, L.; Li, J.; Wang, Z.; Zhao, K.; Yang, C.; Hercule, K. M.; Lin, C.; Shi, C.; Wei, Q.; et al. Low-crystalline iron oxide hydroxide nanoparticle anode for high-performance supercapacitors. *Nat. Commun.* **2017**, *8*, No. 14264.

(7) Sheberla, D.; Bachman, J. C.; Elias, J. S.; Sun, C.-J.; Shao-Horn, Y.; Dincă, M. Conductive MOF electrodes for stable supercapacitors with high areal capacitance. *Nat. Mater.* **2017**, *16*, 220.
(8) Choi, K. M.; Jeong, H. M.; Park, J. H.; Zhang, Y.-B.; Kang, J. K.; Yaghi, O. M. Supercapacitors of nanocrystalline metal−organic frameworks. *ACS Nano* **2014**, *8*, 7451−7457.
(9) Wang, K.-B.; Xun, Q.; Zhang, Q. Recent progress in metal-organic frameworks as active materials for supercapacitors. *EnergyChem* **2020**, *2*, No. 100025.
(10) Wang, X.; Vasileff, A.; Jiao, Y.; Zheng, Y.; Qiao, S. Z. Electronic and Structural Engineering of Carbon-Based Metal-Free Electrocatalysts for Water Splitting. *Adv. Mater.* **2019**, *31*, No. 1803625.
(11) Yang, L.; Shui, J.; Du, L.; Shao, Y.; Liu, J.; Dai, L.; Hu, Z. Carbon-Based Metal-Free ORR Electrocatalysts for Fuel Cells: Past, Present, and Future. *Adv. Mater.* **2019**, *31*, No. 1804799.
(12) Li, J. C.; Hou, P. X.; Liu, C. Heteroatom-Doped Carbon Nanotube and Graphene-Based Electrocatalysts for Oxygen Reduction Reaction. *Small* **2017**, *13*, No. 1702002.
(13) Hoang, V. C.; Dinh, K. N.; Gomes, V. G. Iodine doped composite with biomass carbon dots and reduced graphene oxide: a versatile bifunctional electrode for energy storage and oxygen reduction reaction. *J. Mater. Chem. A* **2019**, *7*, 22650−22662.
(14) Xia, W.; Qu, C.; Liang, Z.; Zhao, B.; Dai, S.; Qiu, B.; Jiao, Y.; Zhang, Q.; Huang, X.; Guo, W.; et al. High-performance energy storage and conversion materials derived from a single metal−organic framework/graphene aerogel composite. *Nano Lett.* **2017**, *17*, 2788−2795.
(15) Xiong, C.; Yang, Q.; Dang, W.; Li, M.; Li, B.; Su, J.; Liu, Y.; Zhao, W.; Duan, C.; Dai, L.; et al. Fabrication of eco-friendly carbon microtubes@ nitrogen-doped reduced graphene oxide hybrid as an excellent carbonaceous scaffold to load MnO_2 nanowall (PANI nanorod) as bifunctional material for high-performance supercapacitor and oxygen reduction reaction catalyst. *J. Power Sources* **2020**, *447*, No. 227387.
(16) Xiong, C.; Li, T.; Zhu, Y.; Zhao, T.; Dang, A.; Li, H.; Ji, X.; Shang, Y.; Khan, M. Two-step approach of fabrication of interconnected nanoporous 3D reduced graphene oxide-carbon nanotube-polyaniline hybrid as a binder-free supercapacitor electrode. *J. Alloys Compd.* **2017**, *695*, 1248−1259.
(17) Li, D.; Li, Y.; Feng, Y.; Hu, W.; Feng, W. Hierarchical graphene oxide/polyaniline nanocomposites prepared by interfacial electrochemical polymerization for flexible solid-state supercapacitors. *J. Mater. Chem. A* **2015**, *3*, 2135−2143.
(18) Zou, Y.; Zhang, Z.; Zhong, W.; Yang, W. Hydrothermal direct synthesis of polyaniline, graphene/polyaniline and N-doped graphene/polyaniline hydrogels for high performance flexible supercapacitors. *J. Mater. Chem. A* **2018**, *6*, 9245−9256.
(19) Zaaba, N. I.; Foo, K. L.; Hashim, U.; Tan, S. J.; Liu, W. W.; Voon, C. H. Synthesis of Graphene Oxide using Modified Hummers Method: Solvent Influence. *Procedia Eng.* **2017**, *184*, 469−477.
(20) Acevedo-Peña, P.; Haro, M.; Rincón, M. E.; Bisquert, J.; Garcia-Belmonte, G. Facile kinetics of Li-ion intake causes superior rate capability in multiwalled carbon nanotube@TiO_2 nanocomposite battery anodes. *J. Power Sources* **2014**, *268*, 397−403.
(21) Ćirić-Marjanović, G. Recent advances in polyaniline research: Polymerization mechanisms, structural aspects, properties and applications. *Synth. Met.* **2013**, *177*, 1−47.
(22) Sapurina, I.; Stejskal, J. The mechanism of the oxidative polymerization of aniline and the formation of supramolecular polyaniline structures. *Polym. Int.* **2008**, *57*, 1295−1325.
(23) Kaniyoor, A.; Ramaprabhu, S. A Raman spectroscopic investigation of graphite oxide derived graphene. *AIP Adv.* **2012**, *2*, No. 032183.
(24) Olejnik, P.; Gniadek, M.; Echegoyen, L.; Plonska-Brzezinska, M. E. Nanoforest: Polyaniline Nanotubes Modified with Carbon nano-Onions as a Nanocomposite Material for Easy-to-Miniaturize High-Performance Solid-State Supercapacitors. *Polymers* **2018**, *10*, No. 1408.
(25) Prosanov, I. Y.; Matvienko, A. A. Study of PVA thermal destruction by means of IR and Raman spectroscopy. *Phys. Solid State* **2010**, *52*, 2203−2206.
(26) Kudin, K. N.; Ozbas, B.; Schniepp, H. C.; Prud'homme, R. K.; Aksay, I. A.; Car, R. Raman spectra of graphite oxide and functionalized graphene sheets. *Nano Lett.* **2008**, *8*, 36−41.
(27) Mažeikienė, R.; Niaura, G.; Malinauskas, A. A comparative multiwavelength Raman spectroelectrochemical study of polyaniline: a review. *J. Solid State Chem.* **2019**, *23*, 1631−1640.
(28) Mažeikienė, R.; et al. Study of redox and protonation processes of polyaniline by the differential multiwavelength Raman spectroelectrochemistry. *Spectrochim. Acta, Part A* **2019**, *221*, No. 117147.
(29) Smith, E.; Dent, G. *Modern Raman Spectroscopy: A Practical Approach*; Wiley, 2019.
(30) Kuznetsov, A. N.; Ayupov, A. B.; Yeletsky, P. M.; Lebedeva, M. V. Influence of monomer content on course of aniline polymerization in presence of high surface area carbon. *J. Electroanal. Chem.* **2019**, *835*, 73−80.
(31) Zhang, K.; Zhang, L. L.; Zhao, X.; Wu, J. Graphene/polyaniline nanofiber composites as supercapacitor electrodes. *Chem. Mater.* **2010**, *22*, 1392−1401.
(32) Gómez, I.; Otazo, E.; Hernández, H.; Rubio, E.; Varela, J.; Ramírez, M.; Barajas, I.; Gordillo, A. Thermal degradation study of PVA derivative with pendant phenylthionecarbamate groups by DSC/TGA and GC/MS. *Polym. Degrad. Stab.* **2015**, *112*, 132−136.
(33) Bharadiya, P.; Jain, R.; Chaudhari, V.; Mishra, S. Graphene oxide-wrapped polyaniline nanorods for supercapacitor applications. *Polym. Compos.* **2019**, *40*, E1716−E1724.
(34) Stobinski, L.; Lesiak, B.; Malolepszy, A.; Mazurkiewicz, M.; Mierzwa, B.; Zemek, J.; Jiricek, P.; Bieloshapka, I. Graphene oxide and reduced graphene oxide studied by the XRD, TEM and electron spectroscopy methods. *J. Electron Spectrosc. Relat. Phenom.* **2014**, *195*, 145−154.
(35) Han, M. G.; Cho, S. K.; Oh, S. G.; Im, S. S. Preparation and characterization of polyaniline nanoparticles synthesized from DBSA micellar solution. *Synth. Met.* **2002**, *126*, 53−60.
(36) Feng, L.; Xia, W.; Wang, T.; Jiang, C.; Gong, H.; Gao, B.; Jiang, Z.; Liu, X.; He, J. Structure stability of polyaniline/graphene nanocomposites in gamma-ray environment. *J. Radioanal. Nucl. Chem.* **2018**, *315*, 627−638.
(37) Golczak, S.; Kanciurzewska, A.; Fahlman, M.; Langer, K.; Langer, J. J. Comparative XPS surface study of polyaniline thin films. *Solid State Ionics* **2008**, *179*, 2234−2239.
(38) Deng, J.; Wang, T.; Guo, J.; Liu, P. Electrochemical capacity fading of polyaniline electrode in supercapacitor: An XPS analysis. *Prog. Nat. Sci.: Mater. Int.* **2017**, *27*, 257−260.
(39) Li, L.; Song, B.; Maurer, L.; Lin, Z.; Lian, G.; Tuan, C.-C.; Moon, K.-S.; Wong, C.-P. Molecular engineering of aromatic amine spacers for high-performance graphene-based supercapacitors. *Nano Energy* **2016**, *21*, 276−294.
(40) Zhao, Y.; Tang, G.-S.; Yu, Z.-Z.; Qi, J.-S. The effect of graphite oxide on the thermoelectric properties of polyaniline. *Carbon* **2012**, *50*, 3064−3073.
(41) Gul, H.; Shah, A.-u.-H. A.; Krewer, U.; Bilal, S. Study on Direct Synthesis of Energy Efficient Multifunctional Polyaniline−Graphene Oxide Nanocomposite and Its Application in Aqueous Symmetric Supercapacitor Devices. *Nanomaterials* **2020**, *10*, No. 118.
(42) Eftekhari, A.; Li, L.; Yang, Y. Polyaniline supercapacitors. *J. Power Sources* **2017**, *347*, 86−107.
(43) Hui, N.; Sun, X.; Niu, S.; Luo, X. PEGylated polyaniline nanofibers: antifouling and conducting biomaterial for electrochemical DNA sensing. *ACS Appl. Mater. Interfaces* **2017**, *9*, 2914−2923.
(44) Hatchett, D. W.; Quy, T.; Goodwin, N.; Millick, N. M. In-situ reduction of Au, Pd, and Pt metal precursors in polyaniline: electrochemistry of variable metal content polymer/metal composites in alkaline solution. *Electrochim. Acta* **2017**, *251*, 699−709.
(45) Fan, M.; An, Y.; Yin, H.; Li, W.; Sun, W.; Lin, Z. Self-assembled reduced graphene oxide/sulfur composite encapsulated by polyaniline

https://dx.doi.org/10.1021/acsaem.0c00361
ACS Appl. Energy Mater. XXXX, XXX, XXX−XXX

for enhanced electrochemistry performance. *J. Solid State Electrochem.* **2018**, *22*, 667−675.

(46) Das, T.; Verma, B. Polyaniline-Acetylene black-Copper cobaltite based ternary hybrid material with enhanced electrochemical properties and its use in supercapacitor electrodes. *Int. J. Energy Res.* **2020**, *44*, 934−949.

(47) Jiang, Y.; Liu, J. Definitions of pseudocapacitive materials: a brief review. *Energy Environ. Mater.* **2019**, *2*, 30−37.

(48) Jiang, H.; Wei, Z.; Ma, L.; Yuan, Y.; Hong, J. J.; Wu, X.; Leonard, D. P.; Holoubek, J.; Razink, J. J.; Stickle, W. F.; et al. An Aqueous Dual-Ion Battery Cathode of Mn_3O_4 via Reversible Insertion of Nitrate. *Angew Chem., Int. Ed.* **2019**, *58*, 5286−5291.

(49) Chao, J.; Yang, L.; Zhang, H.; Liu, J.; Hu, R.; Zhu, M. Engineering layer structure of MoS_2/polyaniline/graphene nanocomposites to achieve fast and reversible lithium storage for high energy density aqueous lithium-ion capacitors. *J. Power Sources* **2020**, *450*, No. 227680.

(50) Aytug, T.; Rager, M. S.; Higgins, W.; Brown, F. G.; Veith, G. M.; Rouleau, C. M.; Wang, H.; Hood, Z. D.; Mahurin, S. M.; Mayes, R. T.; et al. Vacuum-assisted low-temperature synthesis of reduced graphene oxide thin-film electrodes for high-performance transparent and flexible all-solid-state supercapacitors. *ACS Appl. Mater. Interfaces* **2018**, *10*, 11008−11017.

(51) Ye, J.; Wu, Y.-C.; Xu, K.; Ni, K.; Shu, N.; Taberna, P.-L.; Zhu, Y.; Simon, P. Charge Storage Mechanisms of Single-Layer Graphene in Ionic Liquid. *J. Am. Chem. Soc.* **2019**, *141*, 16559−16563.

(52) Ge, M.; Hao, H.; Lv, Q.; Wu, J.; Li, W. Hierarchical nanocomposite that coupled nitrogen-doped graphene with aligned PANI cores arrays for high-performance supercapacitor. *Electrochim. Acta* **2020**, *330*, No. 135236.

(53) Lin, Z.; Waller, G. H.; Liu, Y.; Liu, M.; Wong, C. Simple preparation of nanoporous few-layer nitrogen-doped graphene for use as an efficient electrocatalyst for oxygen reduction and oxygen evolution reactions. *Carbon* **2013**, *53*, 130−136.

(54) Wu, G.; More, K. L.; Johnston, C. M.; Zelenay, P. High-performance electrocatalysts for oxygen reduction derived from polyaniline, iron, and cobalt. *Science* **2011**, *332*, 443−447.

(55) Liu, J.; Zhang, H.; Qiu, M.; Peng, Z.; Leung, M. K.; Lin, W.-F.; Xuan, J. The dimension matters: A review of non-precious-metal single atom nanocatalyst in different structural dimensions for oxygen redox reaction. *J. Mater. Chem. A* **2020**, *8*, 2222−2245.

(56) (a) Jaouen, F.; Proietti, E.; Lefevre, M.; Chenitz, R.; Dodelet, J.; Wu, G.; Chung, H.; Johnston, C.; Zelenay, P. Recent advances in non-precious metal catalysis for oxygen-reduction reaction in polymer electrolyte fuel cells. *Energy Environ. Sci.* **2011**, *4*, 114−130. (b) Bashyam, R.; Zelenay, P. A class of non-precious metal composite catalysts for fuel cells. *Nature* **2006**, *443*, 63−66.

https://dx.doi.org/10.1021/acsaem.0c00361
ACS Appl. Energy Mater. XXXX, XXX, XXX−XXX